- Secondary controls on the stratigraphic signature of the carbon
- 2 isotope excursion marking the Paleocene-Eocene thermal
- maximum at Ocean Drilling Program Site 1135
- 4 Brittany N. Hupp^{1,2*}, D. Clay Kelly¹, Reinhard Kozdon³, Ian J. Orland⁴, John W. Valley^{1,4}
- ¹Department of Geoscience, University of Wisconsin-Madison, Madison, Wisconsin, USA
- 6 ²Department of Atmospheric, Oceanic and Earth Sciences, George Mason University, Fairfax,
- 7 VA, USA

12

18

- 8 ³Lamont-Doherty Earth Observatory of Columbia University, Palisades, NY, USA
- 9 ⁴WiscSIMS, University of Wisconsin-Madison, Madison, Wisconsin, USA
- *corresponding author: bhupp@gmu.edu

13 Final Published Paper:

- Hupp BN, Kelly DC, Kozdon R, Orland IJ, Valley JW (2023) Secondary controls on the stratigraphic signature of the carbon isotope excursion marking the Paleocene-Eocene thermal. Chem. Geol., 632, 11 p. doi.org/10.1016/j.chemgeo.2023.121534
- 19 Key words: carbonate diagenesis, carbon isotope excursion, Paleocene-Eocene thermal
- 20 maximum, planktic foraminifera, secondary ion mass spectrometry

21

Abstract

25

The negative carbon isotope excursion (CIE) associated with an ancient global warming event 26 referred to as the Paleocene Eocene thermal maximum (PETM, ca. 56 Ma) appears smaller in 27 28 marine records than in terrestrial records. This disparity has been attributed to secondary 29 mechanisms that either attenuate or amplify the CIE magnitude in marine and terrestrial records, 30 respectively. Here we investigate the effects of carbonate diagenesis and sediment mixing on the 31 stratigraphic signature of the CIE in a PETM record recovered at Ocean Drilling Program (ODP) 32 Site 1135 in the southern Indian Ocean. Comparison of parallel planktic foraminifer δ^{13} C records 33 constructed with two different analytical techniques – conventional gas source mass 34 spectrometry (GSMS) measurements of individual whole shells versus in-situ microanalyses on 35 subdomains inside individual foraminifer shells using secondary ion mass spectrometry (SIMS) – shows that both of the $\delta^{13}C_{GSMS}$ and $\delta^{13}C_{SIMS}$ records capture the CIE. However, the $\delta^{13}C_{SIMS}$ 36 37 records yield excursion magnitudes (acarininids = 5.3\%, morozovellids = 3.9\%) that are ~1.6\% larger than in the whole-shell $\delta^{13}C_{GSMS}$ records. Patterns of intrashell $\delta^{13}C$ variation delineated 38 by the in-situ SIMS microanalyses indicate that the smaller CIE registered by $\delta^{13}C_{GSMS}$ records is 39 40 chiefly due to measurement of diagenetic calcite by GSMS analyses requiring whole foraminifer 41 shells. We also find that the interiors of many foraminifer shells are infilled with fine-fraction 42 carbonate (nannofossils), and posit that incorporation of non-CIE nannofossils into these infillings further bias whole-shell GSMS δ^{13} C measurements toward higher values over the CIE 43 interval. Thus, infilling of foraminifer shells with reworked fine-fraction carbonate derived from 44 45 non-CIE sediments and carbonate diagenesis combine to attenuate the CIE magnitude in $\delta^{13}C_{GSMS}$ records constructed with whole for aminifer shell analyses. We propose that 5.3%0 is 46 47 the best estimate of the CIE in these marine samples.

49

50

51

52

53

54

55

56

57

58

59

60

61

62

63

64

65

66

67

68

69

70

1. Introduction

The Paleocene-Eocene thermal maximum (PETM, circa 56 Ma) was a transient global warming event closely linked to the release and oxidation of large quantities of isotopicallydepleted carbon in the ocean-atmosphere system (Dickens et al., 1995; Svensen et al., 2004; Higgins and Schrag, 2006; Dunkley Jones et al., 2013; Frieling et al., 2017; Gutjhar et al., 2017; Westerhold et al., 2020; Zeebe and Lourens, 2019). Carbon input during the PETM is signaled by a negative carbon isotope excursion (CIE) in both marine and terrestrial carbon-bearing materials (Kennett and Stott, 1991; Koch et al., 1992; Bowen et al., 2001). A somewhat similar, but more rapid, decrease in the carbon isotope (δ^{13} C) compositions of the atmosphere (Rubino et al., 2013) and surface-ocean (Böhm et al., 2002) is unfolding today as atmospheric carbon dioxide (CO₂) concentrations continue to rise. Thus, the PETM is widely viewed as an informative analogue for gauging the effects of future ocean-climate change driven by human activities (e.g., Zachos et al., 2008; Kirtland-Turner and Ridgwell, 2016, Zeebe et al., 2016; Tierney et al., 2020). However, comparisons of PETM records from different geological settings have shown that the CIE in terrestrial records (3-7‰; avg. 4.7‰) is larger than in correlative marine records (2-3%; avg. 2.8%), raising questions about the true magnitude of δ^{13} C change at the PETM onset (e.g., Bains et al., 2003; Zachos et al., 2007; McInerney and Wing, 2011). Such disparities are problematic because accurate estimates of the true CIE magnitude are needed for modeling PETM carbon-emission scenarios (Ridgwell, 2007; Zeebe and Zachos, 2013; Kirtland Turner and Ridgwell, 2016; Kirtland Turner et al., 2017). Numerous studies have established that the primary stratigraphic signature of the CIE is distorted by such taphonomic processes as carbonate dissolution (Zachos et al., 2005; Pagani et

al., 2006; Bralower et al., 2014), sediment mixing (Ridgwell, 2007; Kirtland Turner et al., 2017; Hupp et al., 2019; Hupp and Kelly, 2020; Hülse et al., 2022), and carbonate diagenesis (Kozdon et al., 2018) in deep-sea sedimentary records of the PETM. Here we follow the analytical and methodological procedures employed by an earlier study (Kozdon et al., 2018) to assess the effects of carbonate diagenesis on the δ^{13} C signature of the CIE in a PETM record recovered at Ocean Drilling Program (ODP) Site 1135 in the southern Indian Ocean (Fig. 1A). To this end, we use secondary ion mass spectrometry (SIMS) to make in-situ δ^{13} C measurements (δ^{13} C_{SIMS}) on various micrometer-scale subdomains within individual planktic foraminifer shells collected from across the CIE interval of the Site 1135 PETM record. Despite being one of a handful of PETM records from the circum-Antarctic region, the Site 1135 record has received scant attention owing to a break in core recovery near the base of its PETM stratigraphy (Coffin et al., 2000). Yet published δ^{13} C records (Jiang and Wise, 2007, 2009) constructed with gas-source mass spectrometry (GSMS) analyses of poly-specific, bulk-foraminifer (>150 µm size fraction) and bulk-carbonate samples indicate that a record of the CIE is captured directly above the coring gap (Fig. 1B). The aforementioned bulk-foraminifer and bulk-carbonate δ^{13} C records (Jiang and Wise. 2007, 2009) delimit the stratigraphic interval over which the CIE is recorded in the Site 1135 PETM section (Fig. 1B), but these records are not well suited for gauging the magnitude of the CIE because they are constructed with samples that consist of varying proportions of different carbonate components (i.e. calcareous nannofossils, planktic and benthic foraminifers), each with its own distinctive δ^{13} C composition (e.g., Bhattacharya et al., 2021). To address this problem, we constructed taxon-specific (genus level) planktic foraminifer δ^{13} C records of the CIE using

 δ^{13} C values measured from individual foraminifer shells by GSMS analyses. The resulting

71

72

73

74

75

76

77

78

79

80

81

82

83

84

85

86

87

88

89

90

91

92

planktic foraminifer $\delta^{13}C_{GSMS}$ records provide a more highly resolved chemostratigraphy for future PETM studies at this climatically sensitive location and, more germane to this study, serve as a reference against which our complementary $\delta^{13}C_{SIMS}$ records can be compared.

2. Materials and Methods

2.1 Study Site and Materials

Ocean Drilling Program Site 1135 (hole A) is located along the southeastern edge of the Kerguelen Plateau in the southern Indian Ocean (**Fig. 1A**) at an intermediate water depth of ~1570 m (Coffin et al., 2000; Jiang and Wise, 2007). Bathymetric constraints based on benthic foraminifer assemblages indicate that the study section was deposited in upper- to mid-bathyal waters (~500-1,000 meters) during the PETM (Schmidt et el., 2018). A stratigraphic series of bulk-sediment samples was taken at 1-cm increments over the lowermost 90 cm of Core 25 (Core 25R-4: 233.25-234.16 mbsf) directly above a coring gap, and an additional 24 bulk-sediment samples were collected from below the coring gap over the uppermost ~65 cm of Core 26 (Core 26R-1: 238.10-238.75 mbsf). The latter series of samples taken from underlying Core 26 is interrupted by a chert nodule centered on ~238.39 mbsf (**Fig. 1B**). Sediments within the study section consist of foraminifer-bearing nannofossil chalk composed of ~95% calcium carbonate (Arney and Wise, 2003), thus the distinctive clay-layer reflecting a transient pulse of increased dissolution found in other deep-sea PETM records was not recovered at Site 1135 due to incomplete core recovery.

Prior to processing samples for foraminifer shells, a small aliquot of each bulk-sediment sample was set aside for GSMS bulk-carbonate δ^{13} C measurements. Bulk-sediment samples were disaggregated in a hydrogen peroxide (10%v) solution, washed over 150 μ m sieve screen,

with resulting residues being oven-dried (75°C) overnight (Jiang and Wise, 2009). Planktic foraminifer shells gleaned from the chalky sediments of the Site 1135 PETM section appear opaque ("frosty") under reflected light and possess thickened, blade-like structures termed muricae (**Fig. 2A, C**). It is also noted that the porous and rough surfaces of many planktic foraminifer shells are infilled with chalky debris consisting primarily of calcareous nannofossils (**Fig. 2A, C**). Individual foraminifers assigned to the genera *Acarinina* spp. and *Morozovella* spp. were hand-picked from the 250-355 μ m size fraction for stable isotope measurements. Acarininid species analyzed include *A. soldadoensis, A. esnaensis,* and *A. angulosa*, while morozovellid species analyzed include *M. subbotinae, M. aequa, M. gracilis,* and *M. acuta*. Previous studies (D'Hondt et al., 1994; Norris, 1996) have shown that the stable isotope signatures of both acarininids and morozovellids are representative of surface-dwelling taxa that inhabited the high- δ 13C waters of the euphotic zone within the oceanic mixed layer (D'Hondt, 1994; Norris, 1996). Thus, the δ 13C compositions of acarininid and morozovellid shells reflect the δ 13C of dissolved inorganic carbon (DIC) in the surface ocean.

2.2 Gas Source Mass Spectrometry (GSMS)

Stable carbon (δ^{13} C) isotope analyses were conducted on individual planktic foraminifer shells collected throughout the study section. A total of 233 single-shell δ^{13} C analyses were performed across 18 stratigraphic samples, with 4 to 17 shells being individually analyzed per stratigraphic sample (Dataset S1). A stratigraphic series of bulk-carbonate samples taken from below the coring gap (Core 26) was analyzed to extend the previously published bulk-carbonate δ^{13} C (δ^{13} C_{bulk}) record farther down-section into the late Paleocene (pre-CIE) interval (Dataset S2; Jiang and Wise, 2009). Conventional gas-source stable isotope measurements were performed at

the University of California – Santa Cruz Stable Isotope Laboratory with a ThermoScientific Kiel IV carbonate device interfaced to ThermoScientific MAT 253 dual-inlet gas-source isotope ratio mass spectrometer (GSMS). External analytical precision for δ^{13} C on this instrument, as determined by replicate analyses of the calcite standard Carrera Marble, was $\leq 0.1\%$ (±2 SD).

2.3 Secondary Ion Mass Spectrometry (SIMS)

In-situ δ^{13} C analyses were performed on micrometer-scale domains inside individual planktic foraminifer shells belonging to the genera *Acarinina* spp. (n = 59 shells) and *Morozovella* spp. (n = 21 shells) using a CAMECA ims-1280 ion microprobe (SIMS) housed in the WiscSIMS Laboratory at the University of Wisconsin-Madison. Planktic foraminifer shells were cast in 25 mm diameter epoxy mounts along with three grains of the WiscSIMS calcite standard UWC-3 (δ^{13} C = -0.91% VPDB, Kozdon et al., 2009), and set under vacuum. All foraminifers were placed within a 10-mm circle, with the UWC-3 calcite grains in the center of the mount to reduce instrumental bias related to sample position (Kita et al., 2009). All planktic foraminifers were oriented in umbilical view prior to being caste in epoxy (**Fig. 2**). The epoxy mounts were polished to midsection with a relief of <1 μ m (Kita et al., 2009). Scanning electron microscope (SEM) images were taken using backscattered electron (BSE) and secondary electron (SE) detectors in order to identify domains for in-situ SIMS analysis. Epoxy mounts were subsequently cleaned with ethanol and DI-water, dried in a vacuum oven overnight, and Au-coated prior to analysis.

In-situ δ^{13} C data were compiled over the course of three separate SIMS sessions: September 2013, February 2018, and July 2018 (**Table 1**; Dataset S3). All δ^{13} C values are reported relative to VPDB (‰). Spot sizes produced by the primary 133 Cs⁺ beam for δ^{13} C analysis were ~10 μ m in diameter and 1 μ m deep. During SIMS δ^{13} C analysis, secondary ions ¹²C, ¹³C, and ¹³CH were detected simultaneously using Faraday cup detectors. One to seven spots were analyzed within the ultimate and/or penultimate chambers of each shell. Four measurements of the UWC-3 calcite standard were conducted prior to and following every ten to twelve shell analyses to correct for instrumental mass fractionation. The reproducibility of the UWC-3 standard analyses was used to determine the analytical precision for the bracketed shell analyses and differed between sessions (Table 1). Secondary ion yield and background-corrected ¹³CH/¹³C was examined relative to the bracketing standards in order to identify analytical outliers. Ratios of ¹³CH/¹³C can be used to detect contamination by water, organic matter, and/or other-H-bearing phases that may influence data quality (Kozdon et al., 2018). Session-specific conditions including primary ion beam intensity, average precision (2SD), and "cutoffs" for relative secondary ion yield and background-corrected CH/C ratios are listed in Table 1. Count rates for ¹²C during session 1 ranged between 4.2 x 10⁶ and 4.9 x 10⁶ counts per second (cps), whereas count rates ranged from $\sim 6 \times 10^6$ and $\sim 8 \times 10^6$ cps for sessions 2 and 3. Analytical time for analysis was approximately 5 minutes which included ~1 minute for presputtering, ~1 minute for automatic centering of secondary ion image, and 20 cycles (8 seconds each) of analysis. Following SIMS analysis, the epoxy mounts received a second Au-coat and were imaged via SEM SE to examine pit location and shape. Irregular pits (Cavosie et al., 2005) and those overlapping cracks, epoxy, or porous regions resulted in omission of associated data points.

182

183

184

163

164

165

166

167

168

169

170

171

172

173

174

175

176

177

178

179

180

181

3. Results

3.1 Carbon Isotope Records

185 3.1.1 Bulk carbonate $\delta^{13}C$ record

The bulk-carbonate δ^{13} C record (Jiang and Wise, 2009) shows that the CIE is recorded over the lowermost ~50 cm of Core 25 (234.12 - 233.60 mbsf) directly above a coring gap, with the main body of the CIE spanning ~27 cm (**Fig. 1B**). The δ^{13} C_{bulk} record for pre-CIE samples yields a mean value of 2.5% (**Fig. 1B**). Unlike other pelagic δ^{13} C_{bulk} records of the CIE, which comprise a series of stepwise decreases that culminate in a CIE minimum value (Bains et al., 1999), the Site 1135 δ^{13} C_{bulk} record exhibits an initial decrease followed by several reversals toward higher values before finally attaining a CIE minimum value. Comparison of the mean pre-CIE value to the CIE minimum (0.1%) in the δ^{13} C_{bulk} record yields an excursion magnitude of ~2.4% (**Fig. 1B**).

3.1.2 Acarininid in-situ SIMS and single-shell GSMS $\delta^{13}C$ records

Parallel carbon isotope records of the CIE were constructed using single-shell GSMS ($\delta^{13}C_{GSMS}$) and in-situ SIMS ($\delta^{13}C_{SIMS}$) analyses on shells belonging to the planktic foraminifer genus *Acarinina* spp. (**Fig. 3**). All in-situ acarininid $\delta^{13}C_{SIMS}$ data, irrespective of intrashell pit location, are shown plotted against the $\delta^{13}C_{bulk}$ curve constructed for the Site 1135 PETM section (**Fig. 3A**). Within the pre-CIE and CIE recovery interval, acarininid $\delta^{13}C_{SIMS}$ values range between ~2‰ and 6‰, and tend to be higher than correlative $\delta^{13}C_{bulk}$ values. By contrast, acarininid $\delta^{13}C_{SIMS}$ values are generally lower than correlative $\delta^{13}C_{bulk}$ values over the CIE interval (**Fig. 3A**). A small subset of in-situ microanalyses performed on acarininid shells yielded intermediate $\delta^{13}C_{SIMS}$ values that fall between pre-CIE and CIE values (**Fig. 3A**).

For comparative purposes, per-shell δ^{13} C averages for acarininids (n = 39) with multiple (>1 pits) SIMS measurements are overlain on the single-shell δ^{13} C_{GSMS} record (**Fig. 3B**). This comparison shows that both records capture the isotopic decrease marking the CIE. As in the

 $\delta^{13}C_{SIMS}$ record, the single-shell acarininid $\delta^{13}C_{GSMS}$ values are higher than correlative $\delta^{13}C_{bulk}$ values within the pre-CIE and CIE recovery intervals but generally lower than correlative $\delta^{13}C_{bulk}$ values over the CIE interval (**Fig. 3B**). However, unlike in the $\delta^{13}C_{SIMS}$ record, no intermediate values are observed over the lower 12 cm of the CIE interval in the single-shell $\delta^{13}C_{GSMS}$ record (**Fig. 3B**). Instead, the distribution of single-shell $\delta^{13}C_{GSMS}$ values is bimodal with readily distinguishable pre-CIE and CIE acarininid shells. Approximately 36% of acarininid shells within this critical 12-cm interval return pre-CIE $\delta^{13}C_{GSMS}$ values that are >2‰.

209

210

211

212

213

214

215

216

217

218

219

220

221

222

223

224

225

226

227

228

229

230

231

Per-sample averages were used to construct complementary carbon isotope records for the acarininid in-situ $\delta^{13}C_{SIMS}$ and whole-shell $\delta^{13}C_{GSMS}$ data (Fig. 3C). The $\delta^{13}C$ data used to calculate sample averages in both of these records were filtered for the following reasons. Reworked shells with pre-CIE values are present within the CIE interval of the in-situ $\delta^{13}C_{SIMS}$ and single-shell $\delta^{13}C_{GSMS}$ records (see Fig. 3B). The inclusion of reworked pre-CIE shells increases sample averages over the CIE interval, which in turn artificially dampens the CIE magnitude registered by both records. To mitigate this taphonomic bias, the two complementary records were 'unmixed' by excluding reworked pre-CIE shells from sample averages over the CIE interval (Fig. 3C). In addition, no shells with intermediate values are observed across the CIE-onset interval of the single-shell $\delta^{13}C_{GSMS}$ record, whereas a handful of shells registered intermediate values in the $\delta^{13}C_{SIMS}$ record (see Fig. 3B). Given that all shells have been altered by diagenesis (see Fig. 2), this discrepancy could reflect the presence of secondary calcite in some of the domains targeted by SIMS microanalysis. As a result, shells registering intermediate values were omitted from per-sample averages over the CIE interval in the in-situ $\delta^{13}C_{SIMS}$ record (**Fig. 3C**). Finally, sample averages used to construct the $\delta^{13}C_{SIMS}$ record are based on shells that have multiple in-situ $\delta^{13}C_{SIMS}$ values (**Fig. 3C**). This precautionary step was taken so

that intrashell $\delta^{13}C$ variability was reasonably well characterized for the shells used to calculate sample averages.

To gauge the CIE magnitude registered by the single-shell $\delta^{13}C_{GSMS}$ and in-situ $\delta^{13}C_{SIMS}$ records, we compare the average value for pre-CIE acarininid shells from below the core gap to the lowest per-sample mean $\delta^{13}C$ value (i.e., CIE minimum) above the core gap. By this definition, comparison of the mean pre-CIE value (3.5‰) to the unmixed CIE minimum (0.14‰) registered by the single-shell $\delta^{13}C_{GSMS}$ record yields a CIE magnitude of about 3.4‰ (**Fig. 3C**). By comparison, the in-situ $\delta^{13}C_{SIMS}$ record tracks the single-shell $\delta^{13}C_{GSMS}$ record over the pre-CIE and CIE recovery intervals, although the in-situ $\delta^{13}C_{SIMS}$ values are generally higher (**Fig. 3C**). Within the CIE interval, however, the per-sample $\delta^{13}C_{SIMS}$ averages are consistently lower than the single-shell $\delta^{13}C_{GSMS}$ per-sample averages. Thus, the CIE magnitude in the $\delta^{13}C_{SIMS}$ record of per-sample averages is 5.3‰, as determined by using a pre-CIE average of 4.0‰ and a CIE minimum of -1.3‰ (**Fig. 3C**).

3.1.3 Morozovellid in-situ SIMS and single-shell GSMS $\delta^{13}C$ records

The $\delta^{13}C$ records for the morozovellids span only the pre-CIE and CIE intervals, as morozovellid shells become exceedingly rare within the overlying CIE recovery interval (**Fig. 4**). All in-situ morozovellid $\delta^{13}C_{SIMS}$ data, irrespective of intrashell pit locations, are shown plotted alongside the complementary $\delta^{13}C_{bulk}$ curve (**Fig. 4A**). Within the pre-CIE interval, in-situ $\delta^{13}C_{SIMS}$ values are variable (~2.5 – 5.5‰) but consistently higher than correlative $\delta^{13}C_{bulk}$ values. By contrast, in-situ morozovellid $\delta^{13}C_{SIMS}$ values are either similar to, or less than, correlative $\delta^{13}C_{bulk}$ values within the CIE interval.

Single-shell morozovellid $\delta^{13}C_{GSMS}$ values are also higher than correlative $\delta^{13}C_{bulk}$ values over the pre-CIE interval (**Fig. 4B**). The offset between single-shell $\delta^{13}C_{GSMS}$ and $\delta^{13}C_{bulk}$ values disappears over the CIE interval where single-shell $\delta^{13}C_{GSMS}$ values converge upon, or are slightly lower than, correlative $\delta^{13}C_{bulk}$ values. Within the CIE interval, the single-shell $\delta^{13}C_{GSMS}$ record reveals that the vast majority of morozovellid shells register CIE values, with only one out of the 68 shells analyzed returning a pre-CIE value (**Fig. 4B**). Also shown are the per-shell mean $\delta^{13}C_{SIMS}$ values for the subset of morozovellids (n = 13) in which multiple in-situ measurements were made (**Fig. 4B**). This comparison shows that the in-situ $\delta^{13}C_{SIMS}$ and single-shell $\delta^{13}C_{GSMS}$ records are in general agreement, with both records capturing the $\delta^{13}C$ decrease marking the CIE.

Carbon isotope records constructed with sample averages for the morozovellid in-situ $\delta^{13}C_{SIMS}$ and single-shell $\delta^{13}C_{GSMS}$ data are shown in **Figure 4C**. Morozovellid shells registering pre-CIE values over the CIE interval were excluded from sample averages, as were shells with only one $\delta^{13}C_{SIMS}$ value. The unmixed single-shell $\delta^{13}C_{GSMS}$ stratigraphy yields a CIE magnitude of only 2.7% (pre-CIE avg. = 3.2%; CIE min. = 0.5%), whereas the unmixed $\delta^{13}C_{SIMS}$ stratigraphy registers a CIE magnitude of ~3.1% (pre-CIE avg. = 3.4%; CIE min. = 0.3%) (**Fig. 4C**).

3.2 Intrashell $\delta^{13}C$ variability

Of the 80 planktic foraminifer shells analyzed by SIMS, multiple in-situ $\delta^{13}C_{SIMS}$ measurements (≥ 2 analysis pits) were successfully made within the ultimate and/or penultimate chambers of 55 specimens (**Fig. 5A, B**). Average intrashell variability (min. – max.) among these 55 shells is 0.82% with a standard deviation of 0.66%. Intrashell variability is consistent between acarininids and morozovellids, but generally greater among pre-CIE shells (1.17% \pm

0.85‰) than in shells from the CIE interval (0.63‰ \pm 0.40‰). Out of the 55 shells with multiple in-situ measurements, 10 shells were found to have intrashell variability greater than twice the analytical precision (2 x 2SD). Of these ten shells, there was either no spatial trend relative to the growth direction of the shell due to both measurements being taken within the same domain (i.e., "indeterminate") or intrashell measurements showed a positive spatial gradient ($\Delta^{13}C_{inner-outer}$) where the $\delta^{13}C_{SIMS}$ value of the inner chamber wall was lower than in the outer edge of the shell or muricae blade (**Fig. 5C, D**). Interestingly, shells showing a positive $\Delta^{13}C_{inner-outer}$ gradient are exclusively from the CIE interval, whereas shells deemed indeterminate with no intrashell gradient were found throughout the PETM section (**Fig. 5D**).

Intrashell $\delta^{13}C_{SIMS}$ variability was also examined for all shells (n=27) with one in-situ measurement located within the chamber wall ($\delta^{13}C_{inner}$) and another in-situ measurement located either on the outer shell edge or clearly within a muricae blade ($\delta^{13}C_{outer}$). A pattern of intrashell $\delta^{13}C_{SIMS}$ variability similar to that found among the shells with statistically significant intrashell variation (2 x 2SD) emerges from this comparison. Specifically, shells within the CIE interval are more likely to exhibit a positive intrashell $\delta^{13}C_{SIMS}$ gradient (**Fig. 6**), where the $\delta^{13}C_{SIMS}$ value of the outer shell edge/muricae blade is higher than in the inner chamber wall. The opposite seems to be the case for the pre-CIE and CIE recovery intervals, where shells appear to be more likely to exhibit a slight negative intrashell $\delta^{13}C$ gradient (**Fig. 6**), because $\delta^{13}C_{SIMS}$ values for the inner shell wall are slightly higher than in the outer shell edge/muricae blades.

4. Discussion

Comparison of parallel δ^{13} C records constructed with conventional GSMS measurements of bulk-carbonate samples (δ^{13} C_{bulk}), individually-analyzed whole planktic foraminifer shells

 $(\delta^{13}C_{GSMS})$, and in-situ SIMS measurements of subdomains within individual planktic foraminifer shells $(\delta^{13}C_{SIMS})$ shows that all three records capture the CIE marking the PETM in the Site 1135 section (**Fig. 3, 4**). However, isotopic offsets between the three $\delta^{13}C$ records seen over the pre- and post-CIE intervals are temporarily reversed over the CIE interval resulting in different CIE magnitudes. For example, $\delta^{13}C$ values from acarininid shells, measured by GSMS or SIMS, are distinctly higher than corresponding $\delta^{13}C_{bulk}$ values over the pre-CIE and post-CIE intervals, while the opposite is true for the CIE interval where acarininid $\delta^{13}C$ values are lower than corresponding $\delta^{13}C_{bulk}$ values (**Fig. 3B, C**). Below, we discuss possible causes of the stratigraphic variation in the offsets seen between our complementary $\delta^{13}C$ records and the potential roles of carbonate diagenesis and sediment mixing in giving rise to differing CIE magnitudes.

4.1 Comparison of GSMS $\delta^{13}C$ records for planktic foraminifers and bulk-carbonate samples

Both the acarininid and morozovellid single-shell $\delta^{13}C_{GSMS}$ records yield a larger CIE magnitude than the parallel $\delta^{13}C_{bulk}$ record (**Fig. 7**). Studies have shown that fine-fraction carbonate (nannofossils), which is the dominant size component of the bulk carbonate record at Site 1135, is more susceptible to sediment mixing than larger carbonate grains such as foraminifer shells (Bard, 2001; Ohkouchi et al., 2002; Paull et al., 1991; Hupp et al., 2019; Hupp and Kelly, 2020). We therefore posit that the smaller CIE magnitude registered by the $\delta^{13}C_{bulk}$ record is due to the upward mixing of pre-CIE nannofossils, which in turn dilutes the amount of CIE carbonate within the CIE interval and attenuates the excursion magnitude in the $\delta^{13}C_{bulk}$ record (e.g., Hupp and Kelly, 2020). The erratic nature of the $\delta^{13}C_{bulk}$ record over the lower part of the CIE interval, where values initially decrease but then fluctuate between positive and

negative shifts before finally reaching a minimum (**Fig. 1B**), most likely reflects varying proportions pre-CIE and CIE materials caused by sediment mixing processes (Hupp and Kelly, 2020). By contrast, $\delta^{13}C_{GSMS}$ measurements performed on individual foraminifer shells permits the identification of reworked specimens with higher pre-CIE values (e.g., **Fig. 3B**) and their exclusion from per-sample mean $\delta^{13}C_{GSMS}$ values over the CIE interval provides a more accurate estimate of the size of the isotopic excursion (**Fig. 3C, 7**).

4.2 Comparison of whole-shell GSMS and in-situ SIMS planktic foraminifer $\delta^{13}C$ records

4.2.1 Differences in CIE magnitude

Comparison of the parallel acarininid $\delta^{13}C$ records shows that sample averages in the insitu $\delta^{13}C_{SIMS}$ record are higher than in the whole-shell $\delta^{13}C_{GSMS}$ record over the pre- and post-CIE intervals (**Fig. 3C**). A similar SIMS-GSMS $\delta^{13}C$ offset ($\Delta^{13}C_{SIMS-GSMS}$) is seen over the pre- and post-CIE intervals in planktic foraminifer (morozovellid) $\delta^{13}C$ records constructed for the PETM section from tropical Site 865 (Kozdon et al., 2018). Such positive $\Delta^{13}C_{SIMS-GSMS}$ offsets likely reflect differences in analyte. For example, $\delta^{13}C_{GSMS}$ analyses of individual foraminifer shells include the juvenile chambers of each specimen, whereas in-situ $\delta^{13}C_{SIMS}$ analyses of discrete subdomains in the ultimate/penultimate chambers exclude analysis of the juvenile chambers of each specimen. We deem this analytical difference significant because the $\delta^{13}C$ of penultimate and ultimate chambers is, on average, ~1% higher than in the juvenile chambers of modern planktic foraminifers that host algal photosymbionts (e.g., Spero and Lea, 1993). Thus, there is a $\delta^{13}C$ increase with the addition of successive chambers to a shell, which results in a positive $\delta^{13}C$ -shell size signal that is also observed in series of size-segregated ancient acarininid and morozovellid shells (e.g., Shackleton et al., 1985; D'Hondt et al., 1993; Norris, 1996). We

therefore posit that the positive $\Delta^{13}C_{SIMS-GSMS}$ offset seen over the pre- and post-CIE intervals (**Fig. 3C**) is, in part, due to the inclusion of $\delta^{13}C$ -depleted juvenile chambers by whole-shell $\delta^{13}C_{GSMS}$ analyses.

Another plausible factor contributing to the positive Δ¹³C_{SIMS-GSMS} offset seen over the pre- and post-CIE intervals is the addition of secondary calcite (diagenesis) precipitated from δ¹³C-depleted bottom waters and interstitial pore fluids, which was included in the whole-shell δ¹³C_{GSMS} analyses but excluded from the in-situ δ¹³C_{SIMS} analyses. Much like at Site 865, planktic foraminifer shells from the Site 1135 PETM section appear opaque ("frosty") under reflected light and possess thickened, blade-like structures termed muricae (**Fig. 2A, C**). These are the telltale signs of carbonate diagenesis (Pearson et al., 2001; Sexton et al., 2006). However, the Site 1135 PETM section was recovered from a deeper burial depth (~234 meters below sea floor, mbsf) than the Site 865 PETM section (~103 mbsf), so the diagenetic histories of these two pelagic PETM records may differ. This assertion is supported by the chalky character of the Site 1135 sedimentary record, which differs from the weakly lithified, calcareous ooze composing the Site 865 PETM section. Hence, the Site 1135 PETM section affords the opportunity to investigate the effects of burial compaction and chalk diagenesis on the stratigraphic signature of the CIE.

However, the sign of the $\Delta^{13}C_{SIMS}$ - $_{GSMS}$ offset is reversed over the CIE interval (**Fig. 3C**). This transient $\Delta^{13}C_{SIMS}$ - $_{GSMS}$ reversal is significant for several reasons. First, both the SIMS- and GSMS-based acarininid $\delta^{13}C$ records capture the CIE (**Fig. 3C**), but the transient $\Delta^{13}C_{SIMS}$ - $_{GSMS}$ reversal results in a larger CIE magnitude in the $\delta^{13}C_{SIMS}$ record (5.3%) than that (3.4%) registered by the single-shell $\delta^{13}C_{GSMS}$ record (**Fig. 7**). Secondly, it contradicts the view that the larger CIE registered by the $\delta^{13}C_{SIMS}$ record is an analytical artifact since such an instrumental

bias would, in theory, yield a systematic $\Delta^{13}C_{SIMS}$ -GSMS offset that is fairly consistent in both its sign and magnitude over the entirety of the Site 1135 stratigraphy. Finally, the transient $\Delta^{13}C_{SIMS}$ -GSMS reversal suggests that processes other than ontogenetic "vital effects" (i.e. photosymbiosis) have altered the stratigraphic signature of the CIE.

369

370

371

372

373

374

375

376

377

378

379

380

381

382

383

384

385

386

387

388

389

390

391

A similar Δ^{13} C_{SIMS}-GSMS</sub> reversal is seen over the CIE and CIE-recovery intervals of the PETM record from tropical Site 865, where seafloor diagenesis was invoked to account for the differing CIE magnitudes registered by the single-shell $\delta^{13}C_{GSMS}$ and in-situ $\delta^{13}C_{SIMS}$ records (Kozdon et al., 2018). In short, it was shown that GSMS analyses requiring whole foraminifer shells measure both diagenetic (i.e., muricae overgrowths) and biogenic calcites, which tends to smooth and attenuate isotopic excursions associated with the PETM (Kozdon et al., 2013, 2018). Tentative evidence for such a diagenetic mechanism influencing the Site 1135 record is provided by the subset of shells from the CIE interval showing a positive intrashell $\delta^{13}C_{SIMS}$ gradient $(\Delta^{13}C_{inner-outer})$ where the inner chamber walls yield lower $\delta^{13}C_{SIMS}$ values than the outer edge/muricae of the shells (Fig. 5, 6). Admittedly, the data are sparse and their significance limited by analytical uncertainty, but it appears that CIE shells are more likely to register a positive intrashell δ^{13} C gradient than non-CIE shells, with some CIE shells (n=5) yielding positive Δ^{13} C_{inner-outer} values more than twice the analytical precision (2 x 2SD) for SIMS measurements (**Fig. 5, 6**). Thus, if the higher $\delta^{13}C_{SIMS}$ values of the outer edge/muricae are representative of diagenetic overprinting, then the measurement of diagenetic calcite would artificially elevate single-shell $\delta^{13}C_{GSMS}$ values within the CIE interval and reduce the size of the isotopic excursion (Fig. 7).

This expression of diagenetic overprinting is not surprising when we consider that shoaling of the lysocline increased dissolution of preexisting sedimentary calcite during the early

stages of the PETM (Zachos et al., 2005; Zeebe et al., 2009; Penman et al., 2014). This brief episode of post-depositional dissolution would have chemically eroded preexisting δ^{13} C-rich carbonate deposited before the CIE (Dickens, 2000; Zachos et al., 2005), which in turn imparted an intermediate δ^{13} C composition to the DIC pools of oceanic bottom waters and interstitial pore waters within the upper reaches of the sediment column. Thus, diagenetic calcite precipitated on the outer surfaces of foraminifer shells on the seafloor would record a similar intermediate δ^{13} C composition (Kozdon et al., 2018).

Furthermore, whole foraminifer shells extracted from this record are likely to have chambers filled with calcareous nannofossils (**Fig. 2**), which potentially contributes non-CIE carbonate to the single-shell $\delta^{13}C_{GSMS}$ measurements of specimens found within the CIE interval. As indicated by the $\delta^{13}C_{bulk}$ record, the incorporated chalk likely contains a significant proportion of non-CIE fine-fraction carbonate, thereby increasing single-shell $\delta^{13}C_{GSMS}$ values to more positive values compared to the in-situ $\delta^{13}C_{SIMS}$ values within the CIE interval. This source of pre-CIE contamination is hard to detect in whole shells with a binocular picking-microscope and has been largely overlooked by most PETM studies, but it could have important implications for CIE records constructed with $\delta^{13}C_{GSMS}$ analyses of whole foraminifer shells, especially if the material has experienced high degrees of burial compaction like that observed in the Site 1135 PETM section. We therefore recommend that, prior to GSMS measurements, foraminifer shells be broken open to expose their interiors and cleaned to remove fine-fraction carbonate infillings.

4.2.2 Intermediate values across the CIE onset

The CIE magnitude is not the only stratigraphic difference observed when comparing $\delta^{13}C_{GSMS} \text{ and } \delta^{13}C_{SIMS} \text{ records. There is a small subset of shells in both the acarininid and}$

morozovellid $\delta^{13}C_{SIMS}$ records that yield intermediate values over the lowermost portion of the CIE interval (**Fig. 3B, 4B**). Multiple in-situ $\delta^{13}C_{SIMS}$ measurements were made in these shells, lending confidence in their intermediate δ^{13} C composition of the ultimate and penultimate chambers. However, acarininids and morozovellids shells measured by GSMS from this same interval yield unimodal or bimodal δ^{13} C values where shells calcified during the pre-CIE and CIE intervals can be clearly differentiated (Fig. 3B, 4B). One explanation for this key difference between records is that the intermediate $\delta^{13}C_{SIMS}$ values actually capture the transition from pre-CIE to CIE conditions directly above the core gap. Most single-shell planktic foraminifer records from the CIE onset yield a distinctly bimodal distribution of single-shell $\delta^{13}C_{GSMS}$ values, with the two modes being centered on readily distinguishable pre-CIE and CIE values (e.g., Kelly et al., 1996; Thomas et al., 2002; Zachos et al., 2007). We find this same bimodal distribution within the acarininid and morozovellid single-shell $\delta^{13}C_{GSMS}$ records of Site 1135 (Fig. 3B), suggesting that the earliest CIE onset has been truncated by dissolution. Moreover, it is unlikely that we would identify multiple shells of intermediate composition via SIMS, and no shells of intermediate composition in the parallel single-shell $\delta^{13}C_{GSMS}$ records. We therefore reject this explanation.

415

416

417

418

419

420

421

422

423

424

425

426

427

428

429

430

431

432

433

434

435

436

Great care was taken to restrict in-situ microanalyses to either the outer shell edge/muricae or chamber wall domains. However, this does not negate the possibility that some 10-µm SIMS pits could overlap a transitional region where both biogenic and diagenetic calcites were simultaneously measured, resulting in intermediate values. Though if this analytical bias were to be responsible, we would expect to find shells of intermediate composition throughout the CIE interval as opposed to being clustered within the earliest CIE interval (Fig. 3B, 4B).

A more tenable explanation is that these shells have been partially to wholly recrystallized and now record intermediate δ^{13} C values as opposed to having only overgrowths of secondary calcite upon muricae nucleation centers. The Site 1135 record is rife with calcareous nannofossils that are particularly prone to sediment mixing and dissolution (Jiang and Wise, 2007, 2009). Partial dissolution of the foraminifer shells upon deposition in combination with dissolution of the chalk-rich section could lead to site-specific patterns of recrystallization in which the shoaling and re-deepening of the lysocline led to partial or whole recrystallization of planktic foraminifer shells. While this process could have affected shells throughout the CIE and latest pre-CIE stratigraphy, this process is most clearly expressed in stratigraphic intervals where overlying and underlying shells have distinctly different δ^{13} C values. For example, in the acarininid $\delta^{13}C_{SIMS}$ record, intermediate values are found both at the CIE onset and at the transition from CIE to earliest recovery interval. Considering the fluctuations in carbonate chemistry during the PETM, in combination with the burial depth of this calcareous nannofossilrich record, dissolution and pressure solution likely contributed to the range of recrystallization patterns (i.e., partial versus whole) found among the Site 1135 foraminifers (Schlanger and Douglas, 1974; Fabricius, 2007). The bimodal distribution of morozovellid $\delta^{13}C_{SIMS}$ values found within the CIE interval compared to the unimodal distribution of morozovellid $\delta^{13}C_{GSMS}$ values (Fig. 4B) further supports the interpretation that the intermediate values are representative of partially to wholly recrystallized foraminifers. The unimodal $\delta^{13}C_{GSMS}$ morozovellid values lie between the two modes of the $\delta^{13}C_{SIMS}$ values, suggesting that the GSMS values are a mixture of biogenic and diagenetic calcites.

437

438

439

440

441

442

443

444

445

446

447

448

449

450

451

452

453

454

455

456

457

458

459

Considering the possible causes for the intermediate $\delta^{13}C_{SIMS}$ values, particularly in the earliest CIE interval, we argue that it is valid to exclude these intermediate values when

calculating the CIE minimum. Removal of these shells recording intermediate values most greatly effects the CIE magnitude recorded by the morozovellid $\delta^{13}C_{SIMS}$ record. When these intermediate values are removed, the CIE_{SIMS} minimum for the morozovellids is -0.5\%, resulting in an adjusted CIE magnitude of 3.9% (Fig. 7). As compiled from the literature (McInerney and Wing, 2011), planktic foraminifer $\delta^{13}C_{GSMS}$ records typically register a CIE magnitude of ~2.7\%, which is appreciably smaller than the CIE magnitude seen in correlative PETM records from terrestrial settings. This discrepancy in the size of the CIE has led some researchers to question the fidelity of planktic foraminifer δ^{13} C records of the CIE (Pagani et al., 2006) as these records may have been compromised by dissolution, diagenesis, and/or sediment mixing. Yet, the CIE magnitudes found within our acarininid and morozovellid SIMS records of 5.3% and 3.9‰, respectively, are more comparable to those found in terrestrial records, suggesting that utilization of in-situ SIMS measurements may help reconcile such taphonomic biases. Not only do our SIMS excursion magnitudes compare more favorably with terrestrial records, but they are in good agreement with other SIMS-based deep sea planktic foraminifer δ^{13} C PETM records (Kozdon et al., 2018).

As such, we argue that in-situ $\delta^{13}C_{SIMS}$ analysis more accurately reflects carbon isotopic change during the PETM than parallel $\delta^{13}C_{GSMS}$ records, and can serve as a critical tool for separating primary paleoenvironmental signals from secondary artifacts in deep-sea carbonate records of abrupt carbon cycle perturbations. However, it is important that multiple in-situ measurements be taken within the final chambers in order to identify the "true" value of the mature chamber walls and identify potential diagenetic domains.

481

482

460

461

462

463

464

465

466

467

468

469

470

471

472

473

474

475

476

477

478

479

480

5. Conclusions

Carbon isotope records constructed with parallel stratigraphic series of bulk-carbonate samples ($\delta^{13}C_{bulk}$), individually analyzed whole planktic foraminifer shells (single-shell $\delta^{13}C_{GSMS}$), and microanalyses within individual planktic foraminifer shells (in-situ $\delta^{13}C_{SIMS}$) from the Site 1135 PETM section yield varying CIE magnitudes. The $\delta^{13}C_{bulk}$ record registers the smallest CIE magnitude (\sim 2.4‰), which is likely an artifact of size-dependent sediment mixing whereby the displacement of $\delta^{13}C$ -rich non-CIE fine-fraction carbonate (nannofossils) into the CIE interval has attenuated the CIE_{bulk} magnitude (Hupp et al., 2019; Hupp and Kelly, 2020). The in-situ $\delta^{13}C_{SIMS}$ records return CIE magnitudes that, on average, are \sim 1.6‰ larger than those registered by correlative single-shell $\delta^{13}C_{GSMS}$ records for the planktic foraminifer genera *Acarinina* spp. and *Morozovella* spp. The larger CIE magnitudes registered by the in-situ $\delta^{13}C_{SIMS}$ records, particularly that of the more-complete acarininids (\sim 5.3‰), are more comparable to CIE magnitudes found in terrestrial PETM records, which helps reconcile disparities reported between marine and continental CIE records (McInerney and Wing, 2011). We thus conclude that 5.3 ‰ is the best estimate for the CIE in these marine samples.

Use of secondary ion mass spectrometry (SIMS) to perform in-situ $\delta^{13}C_{SIMS}$ measurements on isolated, micrometer-scale domains within individual planktic foraminifer shells shows that some shells within the CIE interval possess an intrashell $\delta^{13}C_{SIMS}$ gradient $(\Delta^{13}C_{inner-outer})$ where $\delta^{13}C$ compositions of the outer shell walls and muricae blades protruding from the shell surfaces are ~2% higher than those of the inner shell walls. The higher $\delta^{13}C_{SIMS}$ values measured in the outer shell walls and muricae blades are intermediate between pre-CIE and CIE values, and are considered to be post-depositional products of diagenetic overprinting. The intermediate $\delta^{13}C$ composition of this diagenetic calcite suggests that it is an amalgamate of two inorganic carbon pools, dissolved inorganic carbon (DIC) sourced from $\delta^{13}C$ -depleted

oceanic bottom waters and the post-depositional dissolution of $\delta^{13}C$ -rich carbonate precipitated prior to the CIE onset (Kozdon et al., 2018). Thus, single-shell $\delta^{13}C_{GSMS}$ records requiring whole foraminifer shell analyses are biased by inclusion of diagenetic calcite, which results in intermediate per-shell mean values in the $\delta^{13}C_{SIMS}$ record and an attenuated CIE magnitude in the single-shell $\delta^{13}C_{GSMS}$ records for both the acarininids and morozovellids.

Though in-situ $\delta^{13}C_{SIMS}$ microanalyses on planktic foraminifer shells clearly implicate early diagenesis as a principal cause for attenuating the CIE magnitude, other factors such as (1) the relationship between paleo-bathymetry and degree of carbonate dissolution, (2) infilling of CIE shells with $\delta^{13}C$ -rich fine-fraction carbonate derived from the adjacent non-CIE intervals, and/or (3) carbonate pressure solution (chalk diagenesis) stemming from deep burial depths also play a role in attenuating the CIE magnitude registered by $\delta^{13}C$ records constructed with traditional gas-source mass spectrometry such as the single-shell $\delta^{13}C_{GSMS}$ records presented herein. Thus, studies focused on how carbonate diagenesis may have altered the CIE profile in deep-sea PETM stratigraphies should be conducted on a site-specific basis. Furthermore, studies focused on carbonate diagenesis should be conducted on a site-specific basis and consider how rapid fluctuations in carbonate chemistry can alter the expression of carbon isotope stratigraphies in deep sea records of the abrupt global change events like the PETM.

Data Availability

All datasets presented herein are available in the supplemental information submitted with this manuscript.

Acknowledgements

529	Funding for this research was provided by NSF-OCE 1405224 to D.C.K. and R.K., and student
530	grants to B.H. from the Department of Geoscience at University of Wisconsin-Madison. Specia
531	thanks to Bil Schneider, Brian Hess, Colin Carney, Dyke Andreason, Kouki Kitajima, Noriko
532	Kita, and Céline Defouilloy for technical support. WiscSIMS is supported by NSF (EAR-
533	2004618) and the University of Wisconsin-Madison.
534	
535	References
536	Arney, J.E., Wise, S.W.J., 2003. Paleocene–Eocene Nannofossil Biostratigraphy of ODP Leg
537	183, Kerguelen Plateau. Proc. Oce. Drill. Program. 183 Scientific Results.
538	doi:10.2973/odp.proc.sr.183.014.2003.
539	Bains, S., et al., 1999. Mechanisms of Climate Warming at the End of the Paleocene. Science.
540	285, 724-727. https://doi.org/10.1126/science.285.5428.724.
541	Bains, S., et al., 2003. Marine-terrestrial linkages at the Paleocene Eocene boundary. Geol. Soc.
542	Am. 369, 1–9.
543	Bard, E., 2001. Paleoceanographic implications of the difference in deep sea sediment mixing
544	between large and fine particle. Paleoceanography 16, 235–239.
545	https://doi.org/10.1029/2000PA000537.
546	Bhattacharya, J., et al., 2021. Size-fraction-specific stable isotope variations as a framework for
547	interpreting early Eocene bulk sediment carbon isotope records. Paleocean. Paleoclim. 36,
548	e2020PA004132. https://doi.org/10.1029/2020PA004132.
549	Böhm, F., et al., 2002. Evidence for preindustrial variations in the marine surface water
550	carbonate system from coralline sponges. Geochem. Geophy. Geosys. 3,
551	https://doi.org/10.1029/2001GC000264.
552	Bowen, G.J., et al., 2001. Refined isotope stratigraphy across the continental Paleocene-Eocene
553	boundary on Polecat Bench in the northern Bighorn Basin in Gingerich, P.D. (eds.)
554	Paleocene-Eocene stratigraphy and biotic change in the Bighorn and Clarks Fork Basins,
555	Wyoming, University of Michigan Papers on Paleontology 33, 73-88.
556	Bralower, T.J., et al., 2014. Impact of dissolution on the sedimentary record of the Paleocene-

- Eocene thermal maximum. Ear. Plan. Sci. Let. 401, 70-82.
- 558 https://doi.org/10.1016/j.epsl.2014.05.055.
- Cavosie, A.J., et al., 2005. Magmatic δ^{18} O in 4400-3900 Ma detrital zircons: A record of the
- alteration and recycling of crust in the Early Archean. Ear. Plan. Sci. Let. 235, 663–681.
- 561 https://doi:10.1016/j.epsl.2005.04.028.
- Coffin, M.F., et al., 2000, Proceedings of the Ocean Drilling Program, Initial Reports: Site 1135,
- 563 183. https://doi:10.2973/odp.proc.ir.183.2000.
- D'Hondt, S., et al., 1994. Stable isotopic signals and photosymbiosis in Late Paleocene planktic
- foraminifera. Paleobio. 20, 391-406.
- Dickens, G.R., et al., 1995. Dissociation of oceanic methane hydrate as a cause of the carbon
- isotope excursion at the end of the Paleocene. Paleocea. 10, 965-971.
- Dickens, G.R., 2000. Methane oxidation during the Late Palaeocene Thermal Maximum: Bull.
- 569 Soc. Géol. France 171, 37-49.
- 570 Dunkley Jones, T., et al., 2013. Climate model and proxy data constraints on ocean warming
- across the Paleocene-Eocene Thermal Maximum: Ear. Sci. Rev. 125, 123–145.
- 572 https://doi:10.1016/j.earscirev.2013.07.004.
- 573 Fabricius, I. L., 2007. Chalk: composition, diagenesis and physical properties. Geol. Soc. of
- 574 Denmark Bull. 55, 97-128.
- 575 Frieling, J., et al., 2017. Extreme warmth and heat-stressed plankton in the tropics during the
- Paleocene-Eocene Thermal Maximum: Sci. Adv. 3, https://doi:10.1126/sciadv.1600891.
- 577 Gutjahr, M., et al., 2017. Very large release of mostly volcanic carbon during the Palaeocene-
- Eocene Thermal Maximum. Nature 548, 573–577. https://doi:10.1038/nature23646.
- Hay, W.W., et al., 1999. Alternative Global Cretaceous Paleogeography, in Barrera, E. and
- Johnson, C. (eds.), The Evolution of Cretaceous Ocean/Climate Systems, Geological
- Society of America Special Paper 332, pp. 1-47.
- Higgins, J.A., Schrag, D.P., 2006. Beyond methane: Towards a theory for the Paleocene-Eocene
- 583 Thermal Maximum: Ear. Plan. Sci. Let. 245, 523–537.
- 584 https://doi:10.1016/j.epsl.2006.03.009.
- Hülse, D., et al., 2022. Assessing the impact of bioturbation on sedimentary isotopic records
- through muerical models. Ear. Sci. Rev. 234, 104213.
- 587 https://doi.org/10.1016/j.earscirev.2022.104213.

- Hupp, B., Kelly, D.C., 2020, Delays, Discrepancies, and Distortions: Size-Dependent Sediment
- Mixing and the Deep-Sea Record of the Paleocene-Eocene Thermal Maximum from ODP
- Site 690 (Weddell Sea), Paleocea. Paleoclim. 35, 1–19. https://doi:10.1029/2020PA004018.
- Hupp, B.N., et al., 2019. Effects of size-dependent sediment mixing on deep-sea records of the
- Paleocene-Eocene Thermal Maximum. Geology 47, 749–752.
- 593 https://doi:10.1130/G46042.1.
- Hupp, B.H., et al., 2022. Isotopic filtering reveals high sensitivity of planktic calcifiers to
- Paleocene-Eocene thermal maximum warming and acidification. Proc. Nat. Acad. Sci. 119,
- 596 e2115561119. https://doi.org/10.1073/pnas.2115561119.
- Jiang, S., Wise Jr., S.W., 2007. Abrupt turnover in calcareous-nannoplankton assemblages across
- the Paleocene/Eocene thermal maximum; implications for surface-water oligotrophy over
- the Kerguelen Plateau, southern Indian Ocean. Open-File Report U. S. Geol. Surv., Short
- Research Paper 024, https://doi:10.3133/of2007-1047.srp024.
- Jiang, S., Wise, S.W., 2009. Distinguishing the influence of diagenesis on the paleoecological
- reconstruction of nannoplankton across the Paleocene/Eocene Thermal Maximum: An
- example from the Kerguelen Plateau, southern Indian Ocean. Mar. Micropaleo. 72, 49–59.
- 604 https://doi:10.1016/j.marmicro.2009.03.003.
- Kelly, D.C., et al., 1996. Rapid diversification of planktonic foraminifera in the tropical Pacific
- 606 (ODP Site 865) during the late Paleocene thermal maximum. Geology 24, 423-426.
- 607 https://doi.org/10.1130/0091-7613(1996)024<0423:RDOPFI>2.3.CO;2.
- Kennett, J.P., Stott, L.D., 1991. Abrupt deep-sea warming, paleoceanographic changes and
- benthic extinctions at the end of the Palaeocene. Nature 353, 225-229.
- Kirtland Turner, S., Ridgwell, A., 2016. Development of a novel empirical framework for
- interpreting geological carbon isotope excursions, with implications for the rate of carbon
- injection across the PETM. Ear. Plan. Sci. Let. 435, 1–13.
- 613 https://doi:10.1016/j.epsl.2015.11.027.
- Kirtland Turner, S., et al., 2017. A probabilistic assessment of the rapidity of PETM onset. Nat.
- 615 Com. 8, 1–9. https://doi:10.1038/s41467-017-00292-2.
- Kita, N.T., et al., 2009. High precision SIMS oxygen isotope analysis and the effect of sample
- 617 topography. Chem. Geol. 264, 43-57.

- Koch, P.L., et al., 1992, Correlation between isotope records in marine and continental carbon
- reservoirs near the Palaeocene/Eocene boundary. Nature 358, 319–322.
- 620 https://doi:10.1038/358319a0.
- Kozdon, R., et al., 2009. Intratest oxygen isotope variability in the planktonic foraminifer N.
- 622 pachyderma: Real vs. apparent vital effects by ion microprobe. Chem. Geol. 258, 327–337.
- https://doi:10.1016/j.chemgeo.2008.10.032.
- Kozdon, R., et al., 2013. In situ δ^{18} O and Mg/Ca analyses of diagenetic and planktic
- foraminiferal calcite preserved in a deep-sea record of the Paleocene-Eocene thermal
- 626 maximum. Paleocean. 28, https://doi:10.1002/palo.20048.
- Kozdon, R., et al., 2018. Diagenetic Attenuation of Carbon Isotope Excursion Recorded by
- Planktic Foraminifers During the Paleocene-Eocene Thermal Maximum: Paleoceanography
- and Paleoclimatology 33, 367–380. https://doi:10.1002/2017PA003314.
- McInerney, F.A., Wing, S.L., 2011. The Paleocene-Eocene Thermal Maximum: A Perturbation
- of Carbon Cycle, Climate, and Biosphere with Implications for the Future: Ann. Rev. Ear.
- 632 Plan. Sci. 39, 489–516. https://doi:10.1146/annurev-earth-040610-133431.
- Ohkouchi, N., et al., 2002. Spatial and temporal offsets between proxy records in a sediment
- drift. Science 298, 1224–1227. https://doi:10.1126/science.1075287.
- Pagani, M., et al., 2006. Arctic hydrology during global warming at the Palaeocene/Eocene
- 636 thermal maximum. Nature 442, 671–675. https://doi:10.1038/nature05043.
- Paull, C.K., et al., 1991. 14 C offsets and apparently non-synchronous δ^{18} O stratigraphies between
- 638 nannofossil and foraminiferal pelagic carbonates. Quat. Res. 35, 274–290,
- 639 https://doi:10.1016/0033-5894(91)90073-E.
- Pearson, P.N., et al., 2001. Warm tropical sea surface temperatures in the Late Cretaceous and
- Eocene epochs: Nature 414, 481–487. https://doi:10.1038/35097000.
- Penman, D.E., et al., 2014. Rapid and sustained surface ocean acidification during the Paleocene-
- Eocene Thermal Maximum: Paleocean. 29, 357–369. https://doi:10.1002/2014PA002621.
- Ridgwell, A., 2007. Interpreting transient carbonate compensation depth changes by marine
- sediment core modeling: Paleocean. 22, 1–10. https://doi:10.1029/2006PA001372.
- Rubino, M., et al., 2013. A revised 1000 year atmospheric δ^{13} C-CO₂ record from Law Dome and
- South Pole, Antarctica. J. Geophys. Res. Atmos. 118, 8482-8499. https://
- 648 doi:10.1002/jgrd.50668.

- 649 Schlanger, S.O., Douglas, R.G., 1974. The pelagic ooze-chalk-limestone transition and its
- implications for marine stratigraphy: Spec. Pub. Internat. Ass. Sed. 1, 117-148.
- Schmidt, D., et al., 2018. Strategies in times of crisis insights into the benthic foraminiferal
- record of the Palaeocene-Eocene Thermal Maximum. Phil. Trans. R. Soc. A. 376,
- 653 20170328. http://dx.doi.org/10.1098/rsta.2017.0328.
- 654 Sexton, P.F., et al., 2006. Microstructural and geochemical perspectives on planktic foraminiferal
- preservation: "Glassy" versus "Frosty". Geochem. Geophy. Geosys. 7, 29 p.
- Shackleton, N.J., et al., 1985. Stable isotope data and the ontogeny of Paleocene planktonic
- 657 foraminifera. J. Foram. Res. 15, 321-336.
- Spero, H.J., Lea, D.W., 1993. Intraspecific stable isotope variability in the planktic foraminifera
- 659 Globigerinoides sacculifer: Results from laboratory experiments. Mar. Micropaleo. 22, 221-
- 660 234.
- Svensen, H., et al., 2004. Release of methane from a volcanic basin as a mechanism for initial
- Eocene global warming: Nature 429, 542-545.
- Thomas, D.J., et al., 2002. Warming the fuel for the fire: Evidence for the thermal dissociation of
- methane hydrate during the Paleocene-Eocene thermal maximum. Geology 30, 1067–1070.
- https://doi:10.1130/0091-7613(2002)030<1067:WTFFTF>2.0.CO;2.
- Tierney, J.E., et al., 2020. Past climates inform our future. Science 370, eaay3701.
- 667 https://doi:10.1126/science.aay3701.
- Westerhold, T., et al., 2020. An astronomically dated record of Earth's climate and its
- predictability over the last 66 million years. Science 369, 1383–1388.
- 670 https://doi:10.1126/SCIENCE.ABA6853.
- Zachos, J.C., et al., 2005. Paleoclimate: Rapid acidification of the ocean during the paleocene-
- 672 Eocene thermal maximum. Science 308, 1611–1615. https://doi:10.1126/science.1109004.
- Zachos, J.C., et al., 2007. The Palaeocene-Eocene carbon isotope excursion: Constraints from
- individual shell planktonic foraminifer records. Phil. Trans. R. Soc. A 365, 1829–1842.
- 675 https://doi:10.1098/rsta.2007.2045.
- Zachos, J.C., et al., 2008. An early Cenozoic perspective on greenhouse warming and carbon-
- 677 cycle dynamics. Nature 451, 279-283. https://doi.org/10.1038/nature06588.
- Zeebe, R.E., Lourens, L.J., 2019. Solar System chaos and the Paleocene–Eocene boundary age
- constrained by geology and astronomy. Science 929, 926–929.

680	Zeebe, R.E., Zachos, J.C., 2013. Long-term legacy of massive carbon input to the earth system:
681	Anthropocene versus Eocene. Phil. Trans. R. Soc. A 371.
682	https://doi:10.1098/rsta.2012.0006.
683	Zeebe, R.E., et al., 2009. Carbon dioxide forcing alone insufficient to explain Palaeocene-Eocene
684	Thermal Maximum warming. Nat. Geosci. 2, 576–580. https://doi:10.1038/ngeo578.
685	Zeebe, R.E., et al., 2016. Anthropogenic carbon release rate unprecedented during the past 66
686	million years. Nat. Geosci. 9, 325–329. https://doi:10.1038/ngeo2681.
687	
688	
689	
690	
691	
692	
693	
694	
695	
696	
697	
698	Figures and Tables
699	

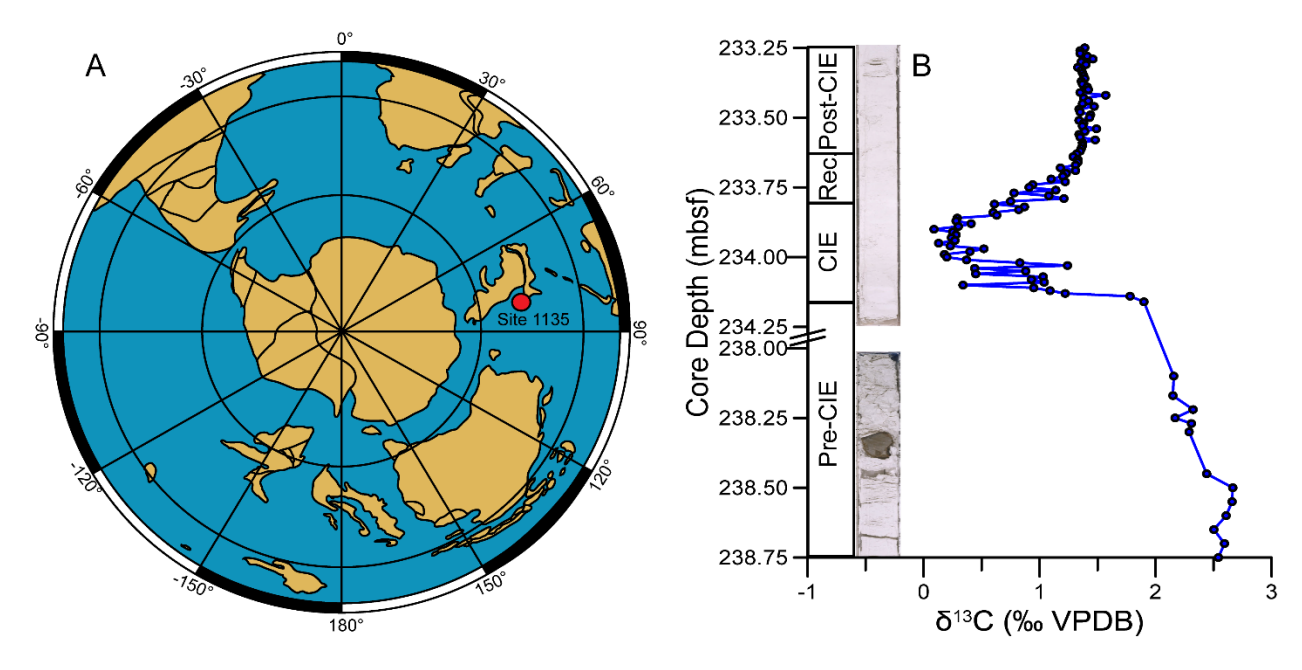


Figure 1. Location of Site 1135 and the negative carbon isotope excursion delimiting the PETM study section. **(A)** Paleogeographic map of circum-Antarctic region (modified from Hay et al., 1999) showing location of Site 1135 circa 56 Ma. **(B)** Core photograph and bulk-carbonate δ^{13} C record showing carbon isotope excursion with pre-CIE, CIE, recovery, and post-CIE intervals delineated. Note carbon isotope record is disrupted by a chert nodule at ~238.30 meters below sea floor (mbsf) and a gap in core recovery just below onset of carbon isotope excursion. Sources for bulk-carbonate data are Jiang and Wise (2009) and this study.

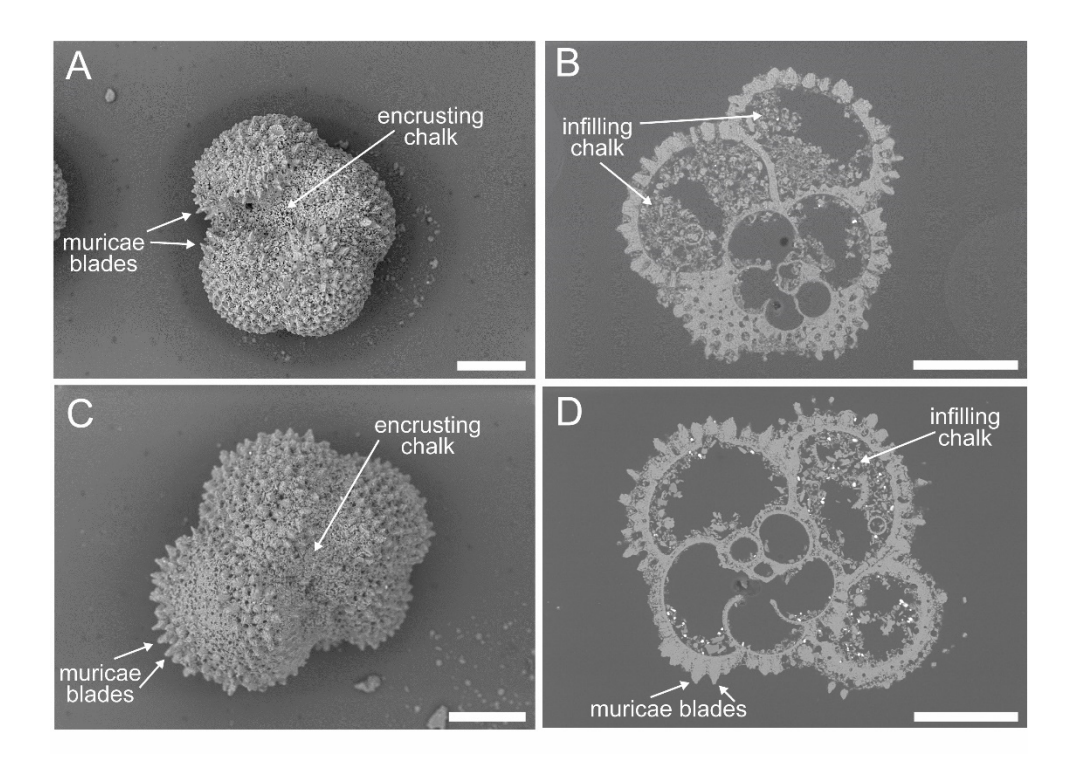


Figure 2. Scanning electron microscope images showing planktic foraminifer preservation in the Site 1135 study section. (A) Exterior of pre-CIE acarininid shell (238.10 mbsf) showing diagenetic blades (muricae) and extraneous chalk infilling umbilical area. (B) Cross-section of same pre-CIE acarininid depicted in panel A showing infilling of chambers by carbonate debris. (C) Exterior of CIE morozovellid shell (234.04 mbsf) showing diagenetic blades (muricae) and extraneous chalk infilling umbilical area. (D) Cross-section of same CIE morozovellid depicted in panel C showing shell interior partially infilled with chalky debris and diagenetic muricae blades. All scale bars = 100 micrometers.

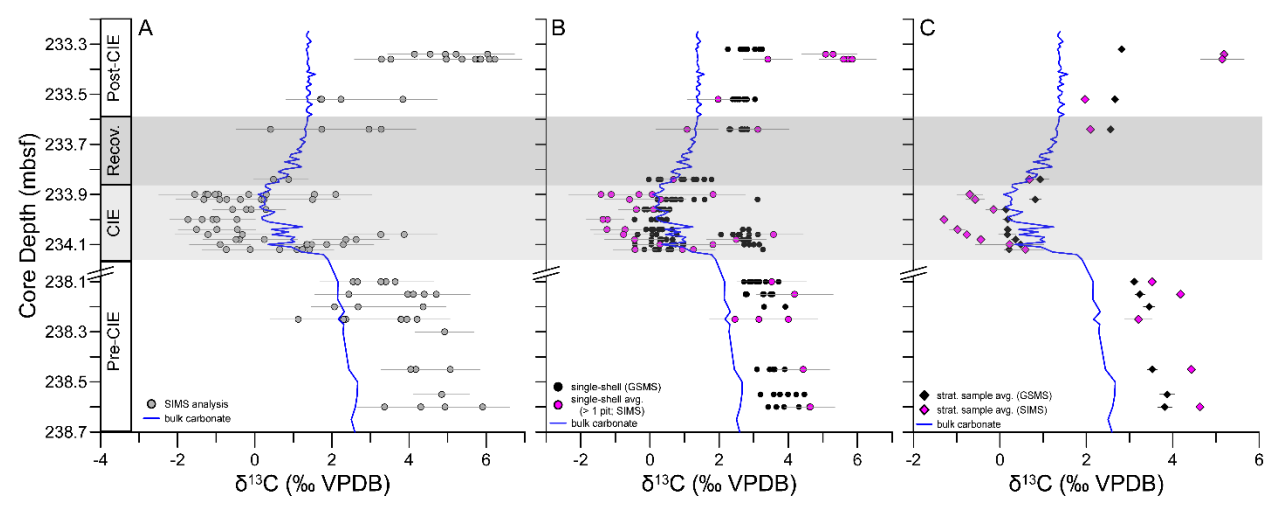


Figure 3. Acarininid and bulk-carbonate $\delta^{13}C$ records showing CIE in Site 1135 PETM section. **(A)** All in-situ $\delta^{13}C_{SIMS}$ values (gray circles) with error bars showing analytical precision (2SD) compared to the $\delta^{13}C_{bulk}$ record (blue line). **(B)** Comparison of the $\delta^{13}C_{bulk}$, single-shell $\delta^{13}C_{GSMS}$ (black circles) and in-situ $\delta^{13}C_{SIMS}$ records (pink circles). All $\delta^{13}C_{SIMS}$ values represent averages for shells with >1 SIMS analyses and gray error bars represent average analytical precision (2SD). Analytical precision for single-shell $\delta^{13}C_{GSMS}$ measurements (2SD) is ≤0.1‰ and not shown. **(C)** "Unmixed" CIE record based on per-stratigraphic sample mean $\delta^{13}C$ values where reworked pre-CIE shells within the CIE interval and shells with intermediate in-situ $\delta^{13}C_{SIMS}$ values from diagenetic muricae are excluded. Only shells with ≥2 intrashell SIMS analyses were included. Error bars for both $\delta^{13}C$ records represent the variability with a given stratigraphic sample (sum of squares).

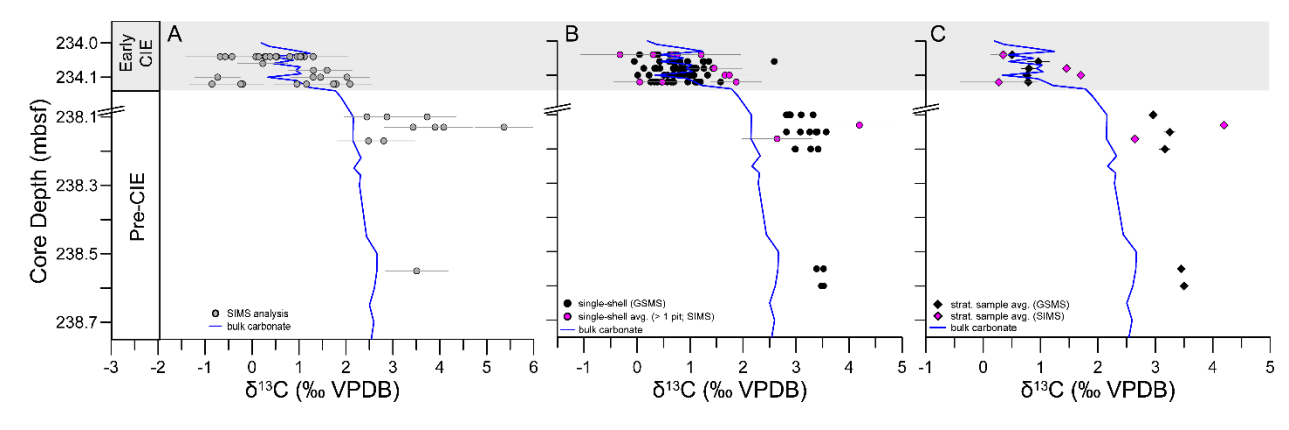


Figure 4. Morozovellid and bulk-carbonate $\delta^{13}C$ records showing the CIE in Site 1135 PETM section. (A) All in-situ $\delta^{13}C_{SIMS}$ values (gray circles) with error bars showing analytical precision (2SD) compared to the $\delta^{13}C_{bulk}$ record (blue line). (B) Comparison of $\delta^{13}C_{bulk}$, single-shell $\delta^{13}C_{GSMS}$ (black circles) and in-situ $\delta^{13}C_{SIMS}$ records (pink circles). All $\delta^{13}C_{SIMS}$ values represent averages for shells with >1 SIMS analyses and gray error bars represent average analytical precision (2SD). Analytical precision for single-shell $\delta^{13}C_{GSMS}$ measurements (2SD) is ≤0.1‰ and not shown. (C) "Unmixed" CIE record based on per-stratigraphic sample mean $\delta^{13}C$ values where reworked pre-CIE shells within the CIE interval are excluded. Only shells with >1 intrashell SIMS analyses were included. Error bars for both $\delta^{13}C$ records represent the variability with a given stratigraphic sample (sum of squares).

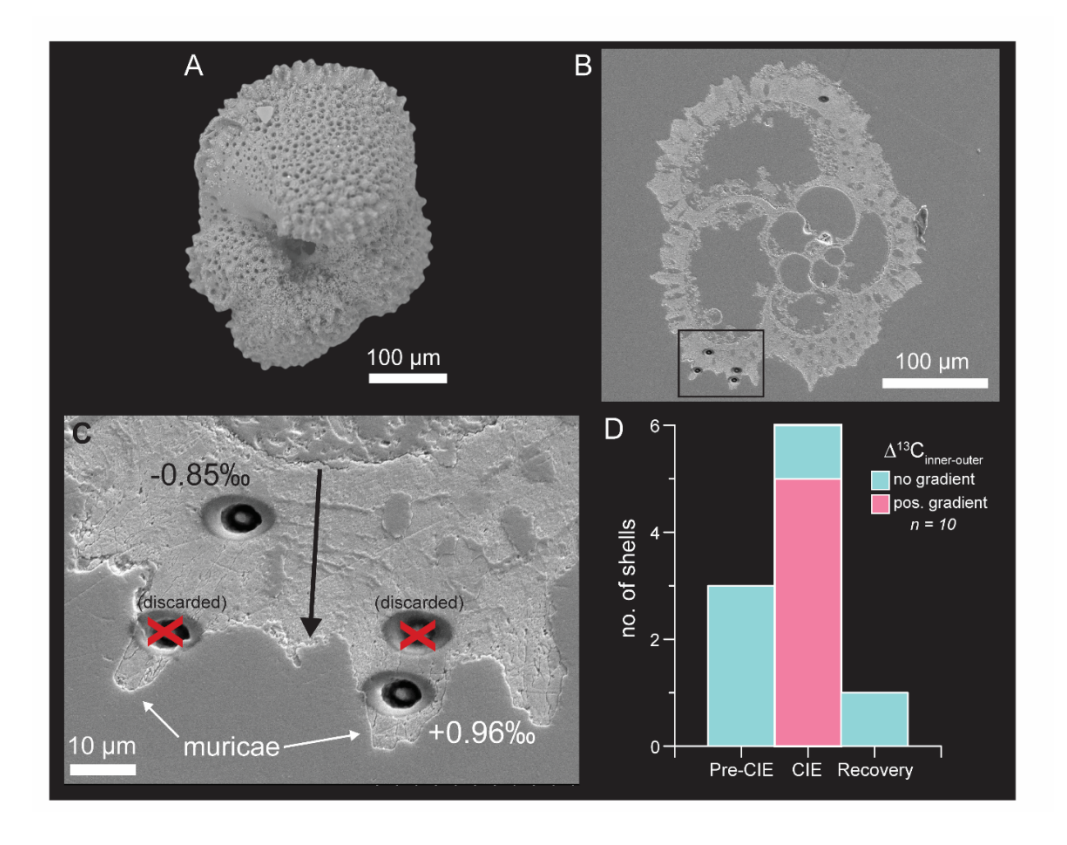


Figure 5. Intrashell carbon isotope variation as shown by in-situ $\delta^{13}C_{SIMS}$ measurements. (A) SEM image of CIE *Morozovella aequa* shell (234.12 mbsf). (B) Cross-section through shell depicted in panel A showing locations of SIMS analysis pits in the penultimate chamber (black box). (C) Highly magnified image showing SIMS analysis pits in penultimate chamber and corresponding $\delta^{13}C_{SIMS}$ values. Red X's denote pits with failed measurements that did not meet relative yield and/or $^{13}CH/^{13}C$ data vetting criteria (see Table 1). The difference between these two measurements ($\Delta^{13}C_{inner-outer} = 1.81\%$) is greater than two times the analytical precision (2SD = 0.49‰) and the spatial trend delineated by these intrashell measurements is an example of a positive gradient, where the outermost muricae blade records a more positive $\delta^{13}C$ value than the inner chamber wall. The black arrow in panel C shows the direction of growth from the inner shell chamber wall to the outer muricae blades. (D) Bar chart showing subset of acarininid and morozovellid shells within the pre-CIE, CIE, and recovery intervals with intrashell $\delta^{13}C_{SIMS}$ variability greater than twice the analytical precision. Blue denotes shells that show an indeterminant intrashell gradient, whereas pink denotes shells with a positive $\Delta^{13}C_{inner-outer}$ gradient.

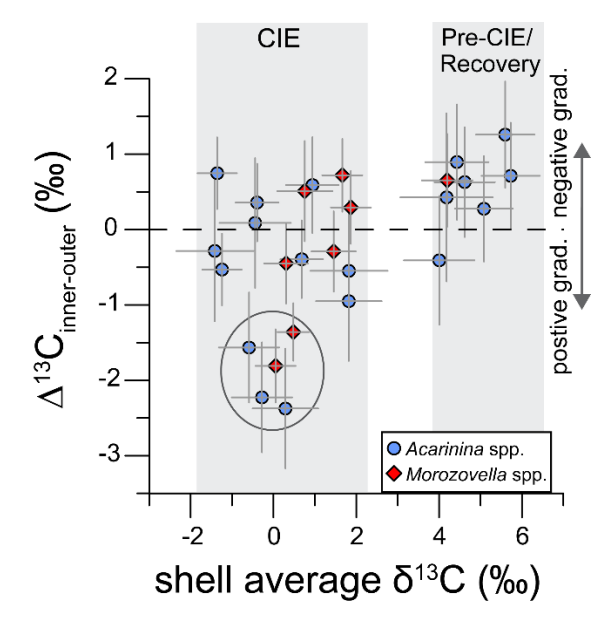


Figure 6. Crossplot showing intrashell $\delta^{13}C$ variation. Comparison of per-shell $\delta^{13}C_{SIMS}$ averages to their differences ($\Delta^{13}C_{inner-outer}$) between $\delta^{13}C_{SIMS}$ values for all shells in which at least one SIMS measurement was made within the inner chamber wall and one SIMS measurement was made on the outer shell edge or muricae blade. Gray error bars demark the analytical precision (2SD) for each shell. Note the higher frequency of shells with positive $\Delta^{13}C_{inner-outer}$ gradients from CIE interval, and that shells with a statistically significant positive $\Delta^{13}C_{inner-outer}$ gradient (circumscribed by the circle) are found exclusively within CIE interval.

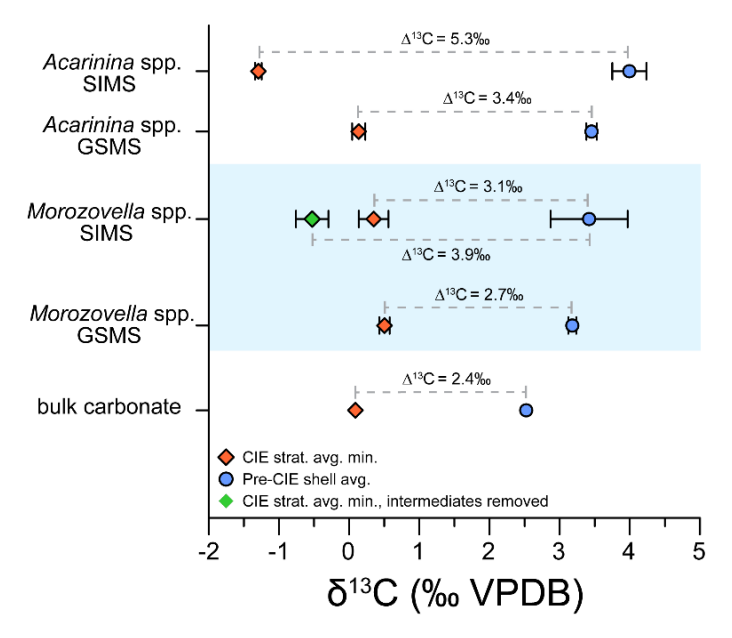


Figure 7. Comparison of CIE magnitudes registered by different δ^{13} C records constructed for Site 1135 PETM section. Average pre-CIE and mean value for sample registering CIE minimum denoted by blue circles and orange triangles, respectively. The green diamond in SIMS-based morozovellid δ^{13} C record denotes mean value of samples registering CIE minimum after intermediate values (~2‰) are removed. Reworked pre-CIE shells not included in calculation of the mean value for samples registering CIE minimum. Error bars for both GSMS and SIMS records express variability within a given stratigraphic sample (SSE).

Table 1. Session-specific δ^{13} C SIMS metadata including time of session, taxa targeted, average beam intensity, average analytical precision, acceptability cutoffs for relative yield, and 13 CH/ 13 C.

Session no.	Session	Taxa Targeted	Beam Intensity (nA)	Precision (avg. 2SD)	Relative Yield Range (%)	¹³ CH/ ¹³ C
1	September 2013	Acarinina spp.	~0.29	± 0.77 ‰	87-102	< 0.035
2	February 2018	Acarinina spp.	~0.42	± 0.72 ‰	91-101	<0.010
3	July 2018	Acarinina spp.; Morozovella spp.	~0.52	± 0.64 ‰	94-101	<0.017